CM² MAGAZINE

第 12 期

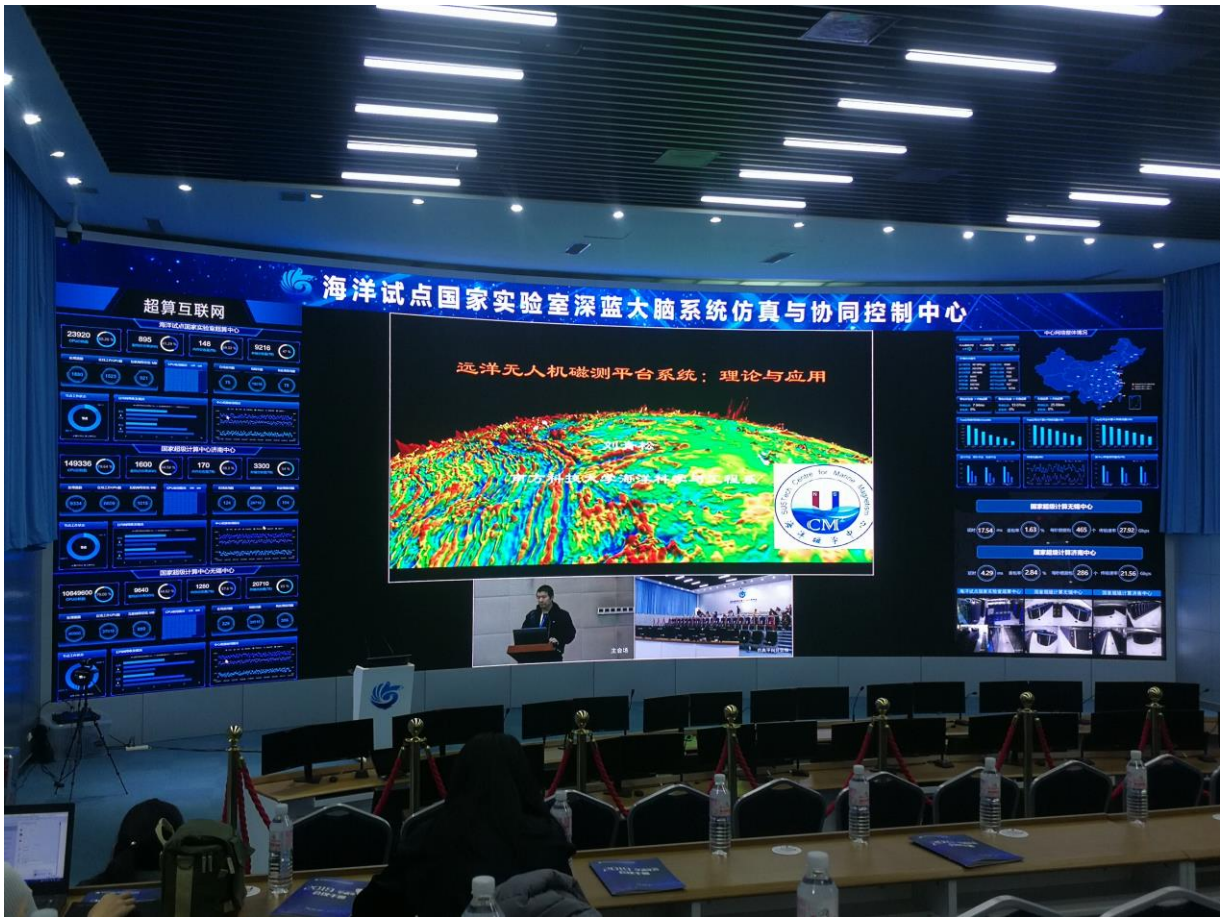

南方科技大学海洋磁学中心主编

创刊词

海洋是生命的摇篮，是文明的纽带。地球上最早的生命诞生于海洋，海洋里的生命最终进化成了人类，人类的文化融合又通过海洋得以实现。人因海而兴。

人类对海洋的探索从未停止。从远古时代美丽的神话传说，到麦哲伦的全球航行，再到现代对大洋的科学钻探计划，海洋逐渐从人类敬畏崇拜幻想的精神寄托演变成可以开发利用与科学研究的客观存在。其中，上个世纪与太空探索同步发展的大洋科学钻探计划将人类对海洋的认知推向了崭新的纬度：深海（deep sea）与深时（deep time）。大洋钻探计划让人类知道，奔流不息的大海之下，埋藏的却是亿万年的地球历史。它们记录了地球板块的运动，从而使板块构造学说得到证实；它们记录了地球环境的演变，从而让古海洋学方兴未艾。

在探索海洋的悠久历史中，从大航海时代的导航，到大洋钻探计划中不可或缺的磁性地层学，磁学发挥了不可替代的作用。这不是偶然，因为从微观到宏观，磁性是最基本的物理属性之一，可以说，万物皆有磁性。基于课题组的学科背景和对海洋的理解，我们对海洋的探索以磁学为主要手段，海洋磁学中心因此而生。

海洋磁学中心，简称 CM^2，一为其全名“Centre for Marine Magnetism”的缩写，另者恰与爱因斯坦著名的质能方程 $E = MC^2$ 对称，借以表达我们对科学巨匠的敬仰和对科学的不懈追求。

然而科学从来不是单打独斗的产物。我们以磁学为研究海洋的主攻利器，但绝不仅限于磁学。凡与磁学相关的领域均是我们关注的重点。为了跟踪反映国内外地球科学特别是与磁学有关的地球科学领域的最新研究进展，海洋磁学中心特地主办 CM^2 Magazine，以期与各位地球科学工作者相互交流学习、合作共进！

“海洋孕育了生命，联通了世界，促进了发展”。 21 世纪是海洋科学的时代，由陆向海，让我们携手迈进中国海洋科学的黄金时代！

目 录

CM^2 快讯

CM^2 师生参加青岛海洋国家实验室 2019 学术年会

2020 年 1 月 11 至 12 日，南科大海洋磁学中心师生一行参加了青岛海洋科学与技术试点国家实验室 2019 学术年会。刘青松教授和仲义博士在年会上做报告，博士生刘伟、王浩森、王敦繁、曹伟参加会议。

刘青松教授做报告

刘青松教授做了《海洋无人机磁测平台系统：理论与应用》的报告，系统介绍了该系统的原理、结构以及性能。传统的海洋磁测包含卫星磁测和船载拖曳式测量两种主要方式。前者分辨率不高，后者的测量效率低。而海洋无人机磁测平台系统的研制成功则兼顾了效率与分辨率，为今后海洋磁测提供了新的方法平台。

仲义博士后做了《多金属结核、结壳在西太平洋及边缘海古气候学中的应用》的报告，向各位同行展示了其最新的研究成果，受到广泛好评。

此次年会集中展示了海洋试点国家实验室试运行以来的不凡成就，彰显了海洋试点国家实验室的使命担当。南科大海洋磁学中心的参会师生均表示收获很大。

古地磁学与岩石磁学冬季国际研讨班正式开班

为促进古地磁学与海洋磁学的发展，2020 年 1 月 13 日，由南方科技大学海洋磁学中心举办的古地磁学与岩石磁学冬季国际研讨班正式开班，会议由周祐民助理教授主持。

与会人员合影

海洋磁学中心主任刘青松教授首先热烈欢迎来自台湾、新加坡、以及全国各高校研究所老师，希望大家能刻苦学习，多相互交流，争取在五天的学习时间里能取得一定的收获，对深圳市和南科大有新的了解。

此次参会人员共计 80 余人。授课老师杨小强教授、周祐民助理教授、林玉峰助理教授以及刘双迟高级工程师也发表了讲话。他们一致认为举办此次冬季学校意义重大，他们将本着一丝不苟的授课态度，为大家讲授各自领域的最新知识，希望大家能学有所获。

此次活动由北京优赛科技公司提供赞助。公司董事长周晓泉表示他对古地磁一直有情怀，非常乐意赞助这样的公益学术活动，期待各位古地磁后辈能够茁壮成长。

相信在各位老师的精心授课下，此次冬季研讨班一定能够取得圆满成功。

文献导读

1. 全球温度变化控制下上新世以来亚洲季风降水变化

翻译人：仲义 zhongy@sustech.edu.cn

Hanlin Wang, Huayu Lu, Lin Zhao et al., ***Asian monsoon rainfall variation during the Pliocene forced by global temperature change [J], Nature Communications,*** *2019, 10(1), 5272. Doi: 10.1038/s41467-019-13338-4.*

摘要：上新世以来亚洲季风变化与全球温度响应还存在争议。本文中我们基于亚洲中部渭河盆地中的植硅体中植物岩指标重建晚中新世以来 C4 植被扩张历史，讨论亚洲季风变化。结果显示在 11 Ma 以来 C4 植被在草地中占主导成分，而在 4Ma 上新世形成后期，以暖-湿为特征的 C4 植被明显降低，而冷-干的 C3 植被开始出现；植物岩的定量化重建指标也显示上新世以来亚洲季风降水明显降低，从 800～1673 mm 降低到 443～900 mm。我们最新记录与前人关于青藏高原隆升导致亚洲季风降水的假说不同，强调出全球温度变化在上新世亚洲季风变化的决定性作用。

ABSTRACT: The Asian monsoon variations under global temperature changes during the Pliocene are still debated. Here we use a sedimentary record of phytoliths (plant silica) from the Weihe Basin, central China, to explore the history of C4 grasses and quantitatively reconstruct the Asian monsoon climate since the late Miocene. Our results show that C4 grasses have been a dominant grassland component since ~11.0 Ma. A subsequent marked decrease in warm- and humid-adapted C4 grasses and an increase in cool- and dry-adapted C3 grasses occurred in the Pliocene, ~4.0 Ma; the phytolith-based quantitative reconstruction of mean annual precipitation marked a decrease from 800~1673 mm to 443~900 mm, indicating a reduction in Asian monsoon rainfall in the Pliocene. Our newly obtained records conflict with the hypothesis that the growth of the Tibetan Plateau strengthened the Asian monsoon rainfall. Nevertheless, they emphasize the importance of global temperature as a determinant of Pliocene Asian monsoon variations.

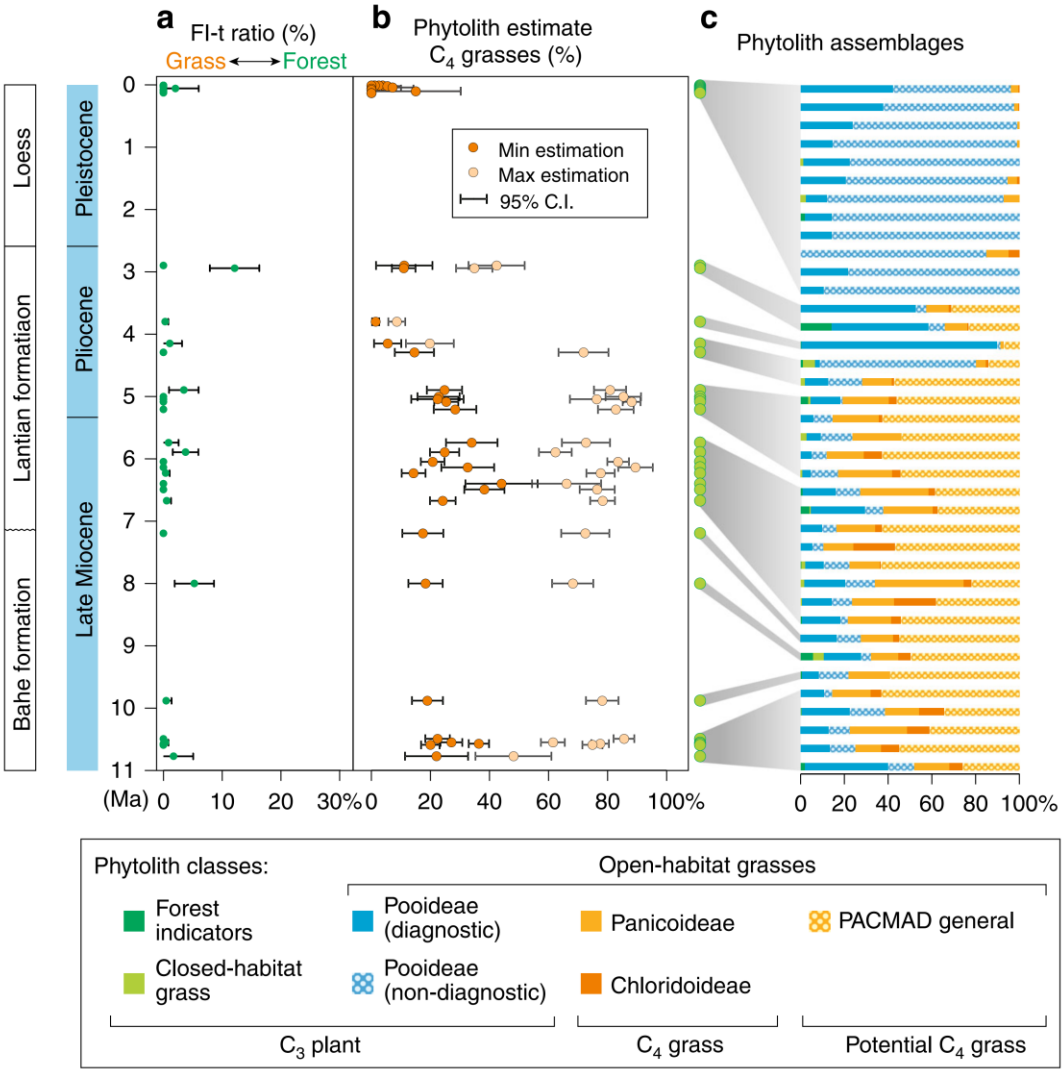

Figure 1. Phytolith records since ~11.0 Ma from Lantian, central China. a Tree cover estimated by phytolith assemblages by comparing forest indicator phytoliths (FI TOT) and diagnostic grass phytoliths (GSSC), FI-t ratio = FI TOT/(FI TOT + GSSC)%. b Potential C4 grasses. The minimum estimation is calculated from PAN + CHLOR (Panicoideae + Chloridoideae) (Eq. 1) and the maximum estimation from PACMAD (a clade of grasses that includes the grass subfamilies Panicoideae–Aristidoideae–Chloridoideae–Centothecoideae–Micrairoideae–Arundinoideae–Danthoniodeae) (Eq. 2). The error bars are calculated from the confidence intervals (95% unconditional case) of each sample using the total count as the sample size. c Phytolith assemblages. For detailed information about these data and equations, see the Methods and Supplementary Table 2.

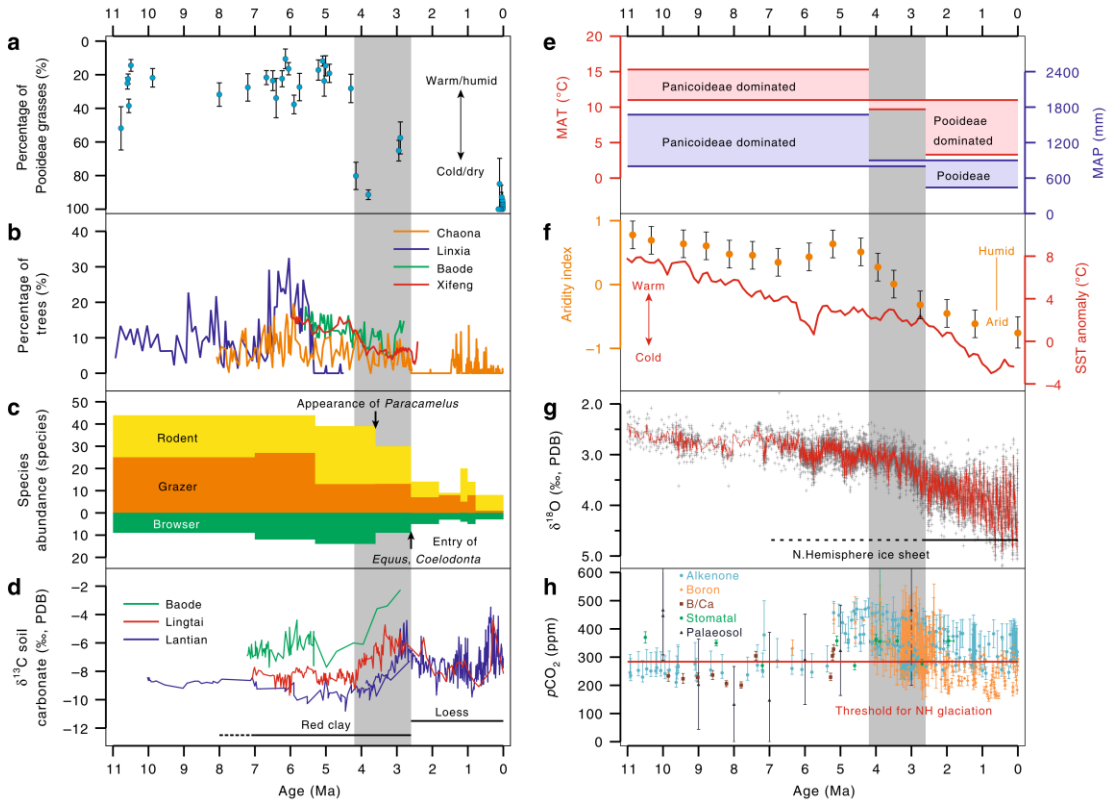

Figure 2. Reconstructed climate change in East Asia and the comparison with sea surface temperature, benthic oxygen isotope and atmospheric CO_2 level since ~11.0 Ma. a The percentage of Pooideae grasses estimated by phytolith assemblages, which were used as a proxy for temperature and/or precipitation. The error bars are calculated from the confidence intervals (95% unconditional case) of each sample using the total count as the sample size. b The percentage of trees derived from palynoflora in Xifeng, Baode, Linxia and Chaona, as a percentage of broadleaf trees of palynoflora. c Species abundance of different types since the late Miocene in northern China. Browsers are large mammals with low-crowned teeth (brachydont) that lived in more humid environments and grazers are large mammals with high-crowned teeth (hypsodont) that lived in more arid conditions. Fossil mammal data of the late Miocene and Pliocene are from Wang et al. and those of the Quaternary are from Xue et al. d Soil carbonate δ13C records from Baode, Lingtai and Lantian. PDB, PeeDee Belemnite. e Phytolith-based quantitative reconstruction of mean annual temperature (MAT) and mean annual precipitation (MAP). f Synthesis of pollen and sedimentary records from northwest China to illustrate the evolution of aridity and the monsoon climate; synthesis of sea surface temperature (SST) anomalies for the Northern Hemisphere (30–50°) based on Uk37 records from four locations. g Benthic 18O composite. h Synthesis of published pCO2 proxy data obtained through a variety of different methodologies. For data sources, see Supplementary Note 3. The grey highlighted intervals indicate the Pliocene cooling (4.2~2.6 Ma) suggested by this study.

2. IODP 的 1236D 孔完整的洋壳样品的岩石磁学特征

翻译人：李园洁 liyj3@sustech.edu.cn

Herrero-Bervera E, Acton G, Krása D, et al. ***Rock magnetic characterization through an intact sequence of oceanic crust, IODP Hole 1256D****[M]//****The Earth's Magnetic Interior****. Springer, Dordrecht, 2011: 153-168.*

摘要：大洋钻探计划（ODP）206 航次和综合大洋钻探计划（IODP）309 和 312 航次在 1256 孔 (6.736º N, 91.934º W, 水深 3635 m)的取钻成功获得了完整洋壳切面的样品，包括地震层 1 的沉积层，层 2 的熔岩和岩墙，层 3 的辉长岩最上层。这个位置的洋壳是大约 15 Ma 之前东太平洋隆起的超快速扩张形成的，全扩张速率>200 mm/yr。对这个完整洋壳切面打钻的一个目标是确定海洋磁异常的来源。对于快速扩张形成的洋壳，磁异常信号主要来自上层的喷出层吗？席状岩墙有任何贡献吗？相对慢速扩张中心辉长岩的磁信号有多重要？什么时候获得磁化强度的？为解决这些问题，我们对整个火成部分做了综合的岩石磁学和古地磁学测量，绘制出沿着钻孔深度磁性矿物颗粒大小，矫顽力，质量归一化的磁化率，居里温度和成分的变化。组成上，我们根据半定量的居里温度分析和显微镜研究，发现氧化铁不同于富钛的钛磁铁矿，通常部分氧化成钛磁赤铁矿，然后到贫钛的磁铁矿。具有不同程度蚀变的钛磁铁矿是整个切面上最常见的磁性矿物，通常被大的硫化铁颗粒包围。低钛的磁铁矿或化学计量上的磁铁矿主要存在于岩墙和辉长岩中，具有比喷出层更高的居里温度（550 ºC 到~ 580 ºC）和更强的矫顽力。磁性颗粒在 Day 图上主要落在假单畴（PSD）磁粒度区域，只有极少量的样品落在单畴（PD）或多畴（MD）区域。这个孔的所有磁学性质受到就位后蚀变的强烈影响，尤其是辉长岩上部到过渡带的部分。岩石磁学数据的一些更显著特征是居里温度随着深度逐渐增加，从喷出层顶部的 200–350 ºC 到过渡带上面的 425 ºC；喷出层上半部分相对下半部分具有更多变的居里温度，更少变化的磁化率和剩磁矫顽力；喷出层具有基本固定的成分(x = 0.6)和氧化铁颗粒(>5νm)的氧化程度(z = 0.6)；喷出层的热磁曲线高度不可逆，冷却曲线比加热曲线具有更高的居里温度(> 500 ºC)； 过渡带岩石磁学性质尤其是居里温度突然变化；席状岩墙相对喷出层和辉长岩，具有更小的颗粒和更高的强度；岩墙和辉长岩居里温度几乎不变（530 ºC 和~ 580 ºC）。

ABSTRACT：Coring at Site 1256 (6.736◦N, 91.934◦W, 3635 m water depth) during Ocean Drilling

Program (ODP) Leg 206 and Integrated Ocean Drilling Program (IODP) Expeditions 309 and 312 successfully sampled a complete section of in situ oceanic crust, including sediments of Seismic Layer 1, lavas and dikes of Layer 2, and the uppermost gabbros of Layer 3. The crust at this site was generated by superfast seafloor spreading (>200 mm/yr full spreading rate) along the East Pacific Rise some 15 Ma ago. One goal of drilling a complete oceanic crust section is to determine the source of marine magnetic anomalies. For crust generated by fast seafloor spreading, is the signal dominated by the upper extrusive layer, do the sheeted dikes play any role, how significant is the magnetic signal from gabbros relative to that at slow spreading centers and what is the timing of acquisition of the magnetization? To address these questions, we have made a comprehensive set of rock magnetic and paleomag- netic measurements that extend through the igneous interval. Continuous downhole variations in magnetic grain size, coercivity, mass-normalized susceptibility, Curie temperatures, and composition have been mapped. Compositionally, we have found that the iron oxides vary from being titanium-rich titanomagnetite (TM60), which are commonly partially oxidized to titanomaghemites, to titanium-poor magnetite as determined semi-quantitatively from Curie temperature analyses and microscopy studies. Skeletal titanomagnetite with varying degrees of alteration is the most com- mon magnetic mineral throughout the section and is often bordered by large iron sulfide grains. The low-Ti magnetite or stoichiometric magnetite is present mainly in the dikes and gabbros and is associated with higher Curie temperatures (550◦C to near 580◦C) and higher coercivities than in the extrusive section. Magnetic grain sizes predominantly fall in the pseudo single domain (PSD) grain size region on Day diagrams, with only a small numbers of samples falling within the single domain (SD) or multi-domain (MD) regions. Overall the magnetic properties of this hole are strongly influenced by post-emplacement alteration, particularly the lower part of the section from the gabbros up into the transition zone. Some of the more prominent features of the rock magnetic data are the gradual increase in Curie temperatures with depth from about 200–350◦C at the top of the extrusives to about 425◦C just above the transition zone, the more variable Curie temperatures and less variable susceptibility and coercivity of remanence in the upper half of the extrusives relative to the lower half the near constant composition (x = 0.6) and oxidation (z = 0.6) of the iron oxide grains (>5vm) in the extrusives (Chapter 12 this volume), the highly irreversible nature of thermomagnetic curves in the extrusives, in which the cooling curve has Curie temperatures higher (generally > 500◦C) than indicated by the heating curve, the abrupt change in

rock magnetic properties across the transition zone, particularly the Curie temperature., a somewhat finer grain size and increased intensity in the sheeted dike zone relative to the extrusives and gabbros, and the nearly constant Curie temperatures (530 and 585◦C) for the dikes and gabbros.

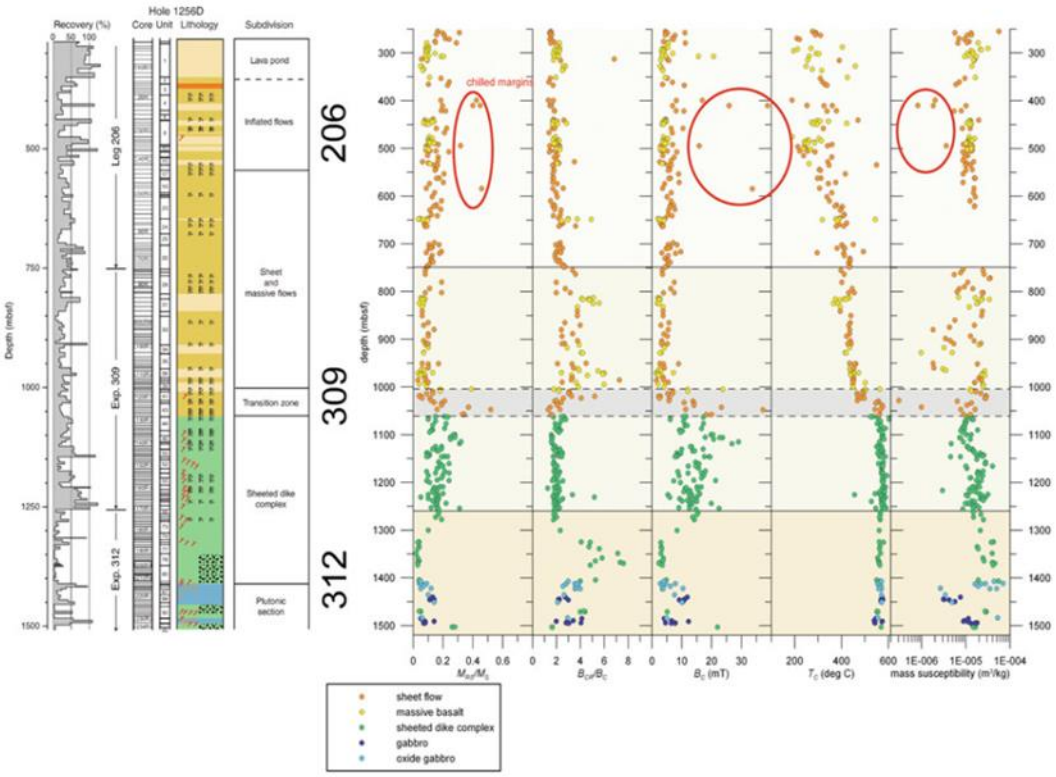

Figure 1. Downhole variation of the rock magnetic results (ratio of saturation remanence over saturation magnetization, coercivity, Curie points and magnetic susceptibility)

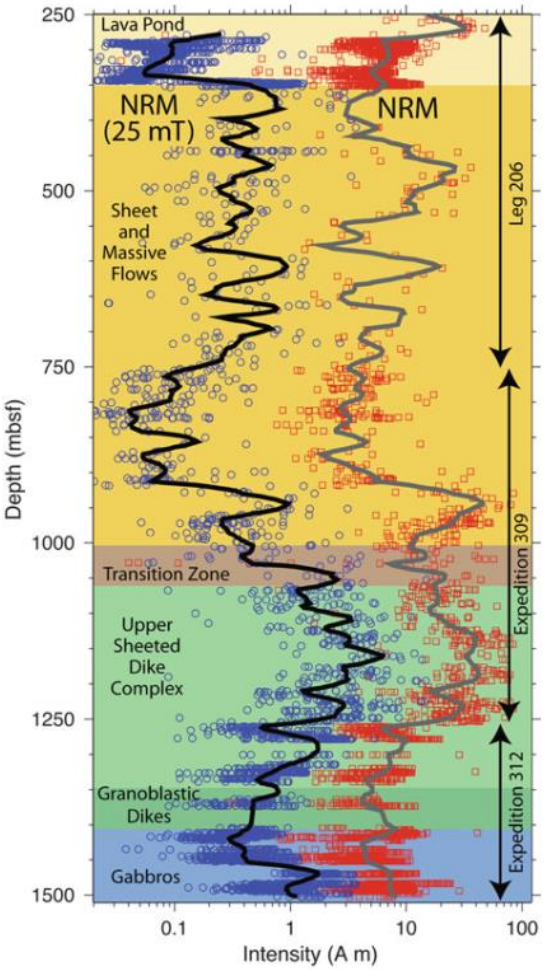

Figure 2. Downhole variation of the NRM intensity before demagnetization (red squares with thick gray curve) and after 25 mT demagnetization (blue circles with thick black curve). The data are from both discrete samples and archive half split-core sections

3. 东亚粉尘颗粒的反应性铁同位素信号：暗示北太平洋深海的铁循环

翻译人：蒋晓东 jiangxd@sustech.edu.cn

Chen, T., Li, W., Guo, B. et al. ***Reactive iron isotope signatures of the East Asian dust particles: Implications for iron cycling in the deep North Pacific****. Chemical Geology [J] (2018), 531, 119342.*

摘要：粉尘的铁释放已经被广泛的认为是海洋初级生产力的重要营养源。粉尘进入海水，反应性铁溶解，将铁同位素信号带入海水中。因此反应性铁的同位素信号能帮助理解全球海洋中铁储库。然而很少有系统性大尺度研究粉尘铁同位素的报导。本研究样品取自在东亚粉尘源区，从跨越上千公里（>3000 Km）的沙漠和黄土取得表层样，用盐酸沥取后获得铁同位素数据。数据表明大多数样品具有相对较小的沥出信号（δ^{56}Fe = –0.09 ± 0.07‰, n=9, 2 SD）。为理解自然颗粒原子促进沥取过程中铁释放的动力学，建立了相对于易溶解性铁和硅酸盐铁不同溶解动力学的模型。通过对两个取自北太平洋的沉积物样品进行持续沥取来检测模型。当引入一个可调谐参数（即初始铁氢氧化物的初始溶解率），其他参数被溶解动力限制，模型成功重现了沥取物 δ^{56}Fe 的演化，并且与来自海洋沉积样品中不同类铁相当一致。因此我们认为沥取过程能被我们的动力学模型模拟，而初始沥取物的铁同位素受控于易溶解铁的端元组成。在沙漠或黄土这样的大陆硅酸盐物质中，这样小但显著的铁同位素分馏记录了氧化环境中风化过程铁的二次形成信号。北太平洋沉积物的初始沥取物相较于东亚沙漠黄土沉积物具有显著轻的铁同位素组成，表明粉尘反应性组分与海水溶解性组分具有明显的同位素转变。沉积的轻的反应性铁同位素信号反过来指向源区的贡献，即低 δ^{56}Fe 的北太平洋深水或者优先被海水配体摄取的 δ^{56}Fe，这些配体来自粉尘反应性组分尤其海水沉积物反应界面。

ABSTRACT：Iron released from wind-blown dust has been widely suggested to be an important nutrient source for oceanic primary productivity. Once introduced into the seawater, the reactive Fe might get dissolved and impart its isotope signature into the water column. Characterization of the reactive iron isotope signatures of eolian dust will thus help to understand the budget of Fe in the global ocean. Yet, there are few systematic studies on the Fe isotope systematics of the dust sources across large spatial scale. Here, we report Fe isotope data from HCl leaching experiment on surficial samples from deserts and loess deposits of different locations spanning > 3000 km spatially in east Asia, one of the most important dust source regions. Our data suggest most of the samples have

relatively similar leaching signatures (δ56Fe = –0.09 ± 0.07‰, n=9, 2 SD). To understand the kinetics of Fe release during proton promoted leaching of natural particles, a synthetic model taking into account of different dissolution dynamics of easily dissolvable Fe and silicate Fe was developed. The model was tested by continuous leaching of two representative pelagic sediment samples recovered from core LL44-GPC3 in the North Pacific. When introducing only one tunable parameter (i.e., the initial dissolution rate of Fe from hydro (oxides), with other parameters constrained by the dissolution kinetics), the model successfully reproduces leachate δ56Fe evolution and agrees reasonably well with Fe speciation in the studied marine sediment samples. We thus suggest that the leaching process can be well characterized by our kinetic model, while Fe isotopes in the initial leachates of the samples are dominated by endmember composition of the easily dissolvable Fe species. The small but distinct fractionation of Fe isotopes in the desert/loess samples from the parental upper continental silicate materials are suggested to record signatures of the secondary Fe species produced during weathering in the oxic environment. The significantly lighter Fe isotope compositions in the initial leachates of the North Pacific pelagic sediment samples compared to the east Asian desert/loess deposits indicate apparent isotope exchange of the dust reactive components with seawater dissolved species. The sedimentary light reactive Fe isotope signatures in turn point toward the contribution of sources characterized by low δ56Fe to the deep North Pacific and/or preferential uptake of δ56Fe by seawater ligands from the dust reactive components particularly at the seawater-sediment interface.

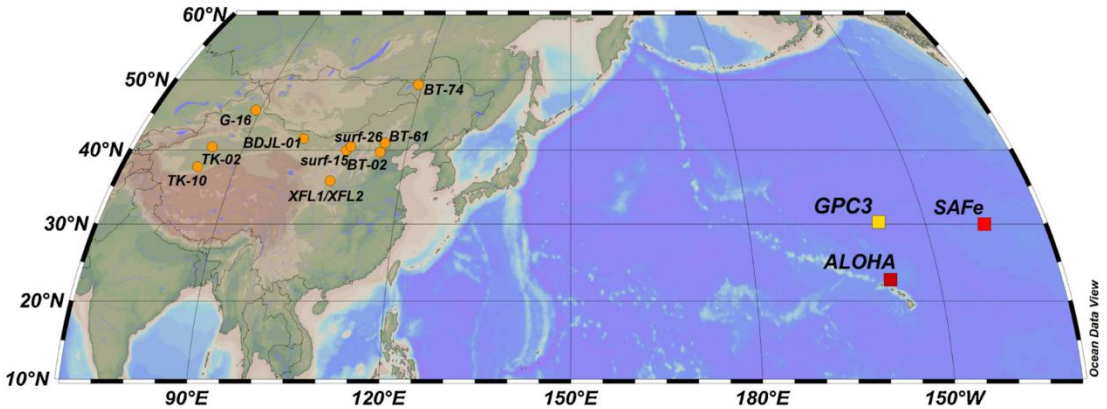

Figure 1. Map showing the locations of the samples of this study. Also shown are the seawater stations of North Pacific that will be mentioned in the discussion.

4. 岩石圈厚度控制大陆玄武岩的成分：以中国东部新生代玄武岩为例

翻译人：冯婉仪 fengwy@sustech.edu.cn

Guo P Y, Niu Y L, Sun P, et al. ***Lithosphere thickness controls continental basalt compositions: An illustration using Cenozoic basalts from eastern China****[J].* ***Geology****, 2020. https://doi.org/10.1130/G46710.1*

摘要：近年来的研究表明，岩石圈厚度的变化对全球海底玄武岩的成分起主要的控制作用。如果这种控制机制（即岩石圈盖效应）确实存在，岩石圈厚度的变化也必然影响在大陆环境下形成的玄武岩组成。为了验证这一假设，我们选择研究中国大陆东部的新生代玄武岩，它们沿着东南-西北向、长约 260 km 的剖面分布，这个剖面地形坡度陡峭（从高于海平面~ 500 m 变化到高于海平面~ 1500 m），反映了该地区岩石圈厚度梯度变化较大（从~ 80 km 变化到 ~ 120 km)。与在西部厚的岩石圈上喷发的玄武岩相比，在东部薄的岩石圈上喷发的玄武岩熔融压力更低（如：具有更高的 Si_{72}、更低的 Mg_{72}、Fe_{72} 和$[Sm/Yb]_N$ 值；下标“72”指的是对全岩主量元素进行分馏效应校正，使其标准化为 Mg# = 72；N-原始地幔标准化）以及熔融程度更高（如：具有低的 Ti_{72}、P_{72}、K_{72}、Rb、Ba、Th、$[La/Sm]_N$、Ba/Zr 和 Zr/Yb 比值）。重要的是，这些地球化学参数均与岩石圈厚度和地形高程呈显著的相关性。这些一阶的观测是岩石圈盖效应的直接表现。岩石圈的混染和地幔源区成分的变化确实会导致这些大陆玄武岩的成分变化，但这些作用的影响会被相互抵消，并且会被岩石圈盖效应所掩盖。这一发现强调了在解释大陆玄武岩的岩石成因和地幔动力学之前评估岩石圈盖效应的重要性。我们的结果还表明，大陆地表高程在地幔深度大于岩石圈-软流圈边界的地方是均衡的。

ABSTRACT: Recent studies demonstrate that lithosphere thickness variation exerts the primary control on global seafloor basalt compositions. If the mechanism of such control, i.e., the lid effect, is indeed at work, lithosphere thickness variation must also influence basaltic compositions in continental settings. To test this hypothesis, we chose to study Cenozoic basalts in eastern continental China over a distance of ~260 km along a southeast-to-northwest traverse with a steep topographic gradient (~500 to ~1500 m above sea level) mirrored with a steep lithospheric thickness gradient (~80 to ~120 km). The basalts erupted on the thinned lithosphere to the east are characterized by lower pressure (e.g., higher Si_{72}, lower Mg_{72}, Fe_{72}, and $[Sm/Yb]_N$; subscript “72”

refers to corresponding oxides corrected for fractionation effect to Mg# = 72; N-primitive mantle normalized) and higher extent (e.g., low Ti_{72}, P_{72}, K_{72}, Rb, Ba, Th, and ratios of more- to less-incompatible elements such as $[La/Sm]_N$, Ba/Zr, and Zr/Yb) of melting than basalts erupted on the thickened lithosphere to the west. Importantly, these geochemical parameters all show significant correlations with both lithosphere thickness and topographic elevation. These first-order observations are a straightforward manifestation of the lid effect. Lithospheric contamination and mantle-source compositional variation can indeed contribute to the compositional variability of these continental basalts, but these latter effects are averaged out and are overshadowed by the lid effect. This finding emphasizes the importance of evaluating the lid effect before interpreting the petrogenesis of continental basalts and mantle dynamics. Our results also indicate that the continental surface elevation is isostatically balanced above a mantle depth that is deeper than the lithosphere-asthenosphere boundary.

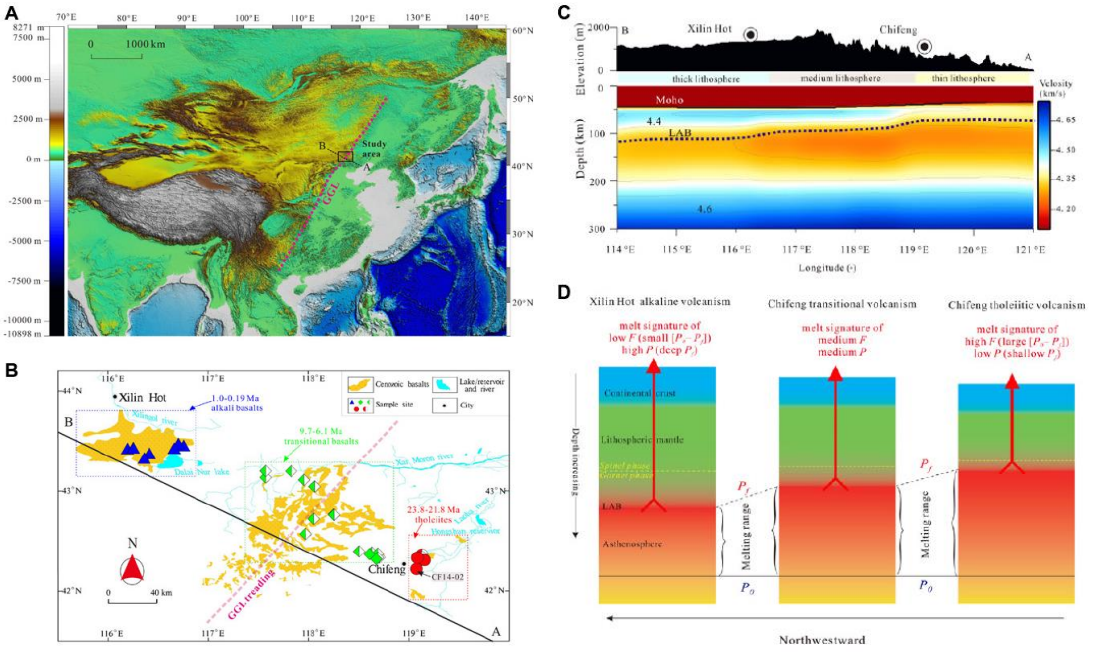

Figure 1. (A) Topographic map of East Asia (data from Amante and Eakins, 2009). "Great Gradient Line" (GGL) is indicated as purple dashed line, which contrasts high elevation and thickened lithosphere to the west from low-elevation and thinned lithosphere to the east. Study area is indicated with a rectangle, with the A-B traverse used in subsequent figures. (B) Distribution and sample locations of Chifeng-Xilin Hot Cenozoic basalts. Solid blue triangles, solid green diamonds, and solid red circles represent sample locations in this study. Half-filled diamonds and half-filled circles represent transitional basalt locations from the literature (Wang et al., 2015; Guo et al., 2016; Pang et al., 2019). (C) Top: Topographic profile along the A-B section in A. Bottom: Vertical section of shear-wave velocity tomography along the A-B traverse (based on data of Li et al., 2013). LAB-lithosphere-asthenosphere boundary. (D) Cartoon illustrating lithosphere thickness control on the geochemistry of erupted basaltic magmas. F-extent of

melting; P-melting pressure; P_f-depth of melting cessation and melt extraction when the decompression-melting mantle encounters the lithosphere, that is, the depth of the lithosphere-asthenosphere boundary; P_0-initial depth of melting when the adiabatically upwelling asthenospheric mantle intersects the solidus.

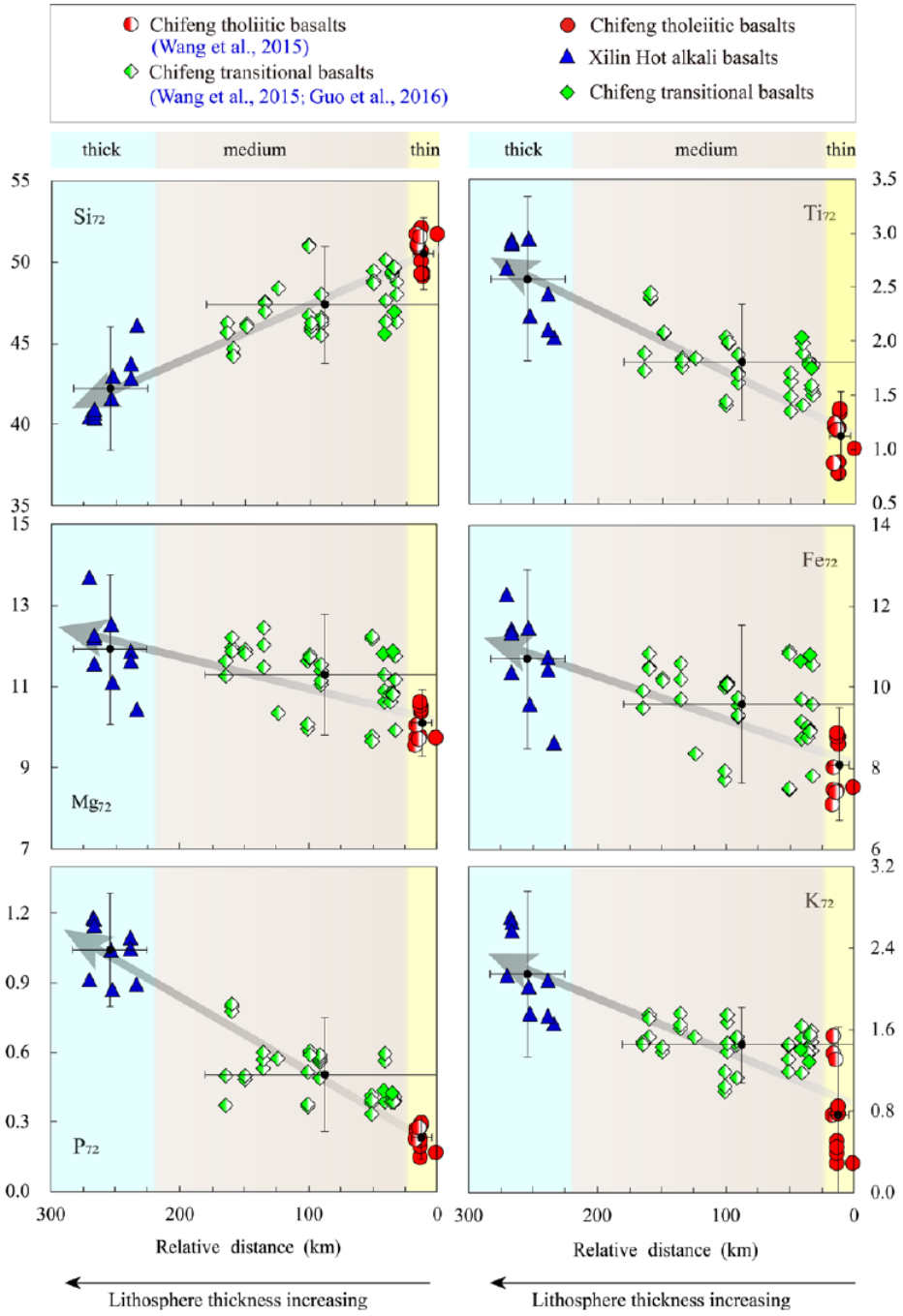

Figure 2. Systematic variation of major element compositions of Chifeng-Xilin Hot (eastern China) Cenozoic basalts as a function of distance relative to the location of sample CF14-02 parallel to the A-B traverse (Fig. 1B). Relative distance is calculated following the method of Niu and Batiza (1993). Black circles represent average composition, with error bars of 2 standard deviations. Subscript "72" refers to corresponding oxides corrected for the fractionation effect to Mg# = 72 (Humphreys and Niu, 2009) so as to facilitate discussion of mantle sources and processes. Three bands with different colors indicate thick, medium, and thin lithosphere at the time of basalt eruption. Symbols are as in Figure 1B.

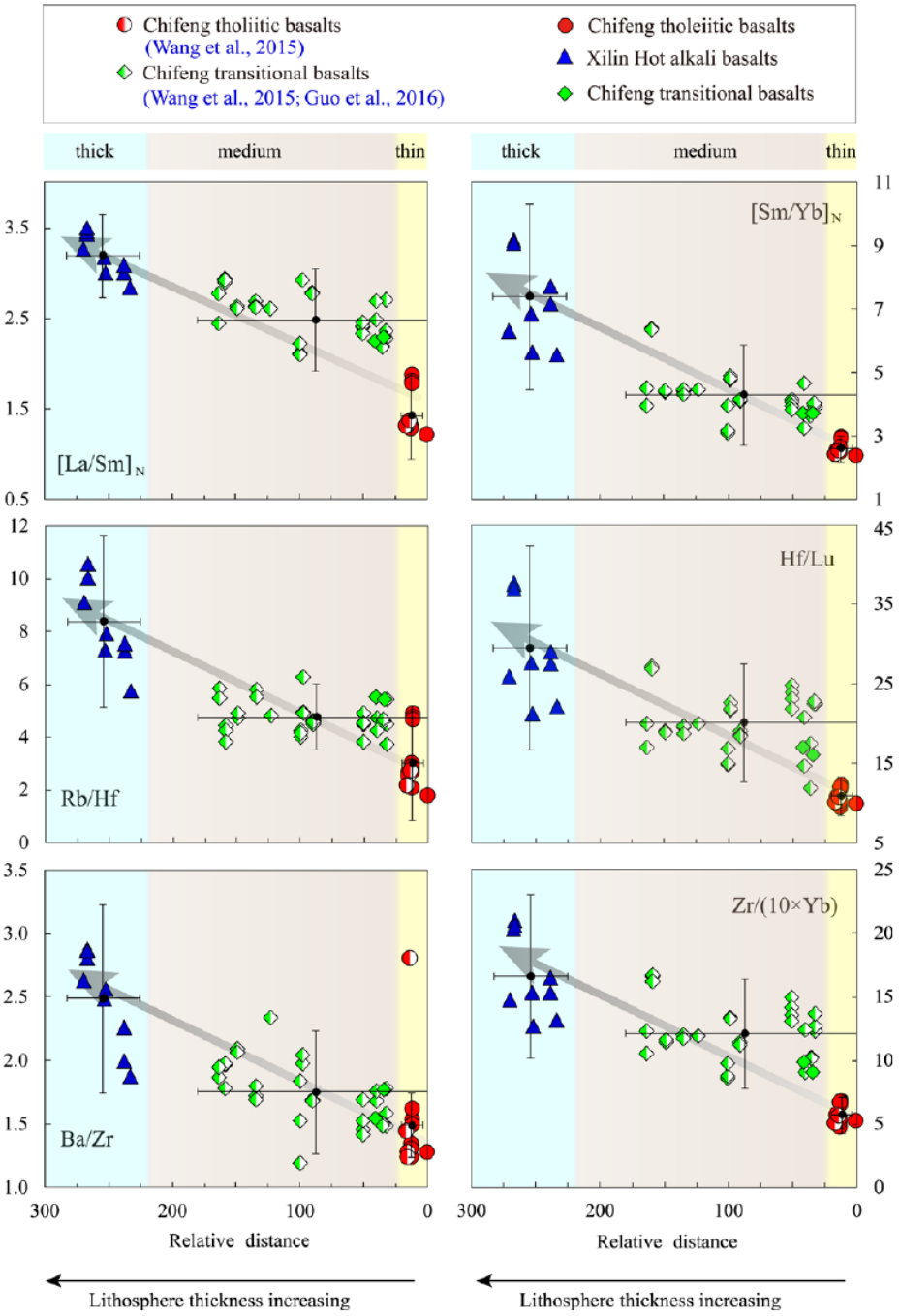

Figure 3. Systematic variation of ratios of more- to less-incompatible elements of Chifeng-Xilin Hot (eastern China) Cenozoic basalts plotted as function of distance from the location of sample CF14-02 as in Figure 2. Black circles represent average composition, with error bars of 2 standard deviations. Subscript N represents primitive mantle normalized.

5. 南冰洋对大气二氧化碳上升的贡献的变化

翻译人：杨会会 11849590@mail.sustech.edu.cn

A D Moy, M R Palmer, W R Howard, et al. ***Varied contribution of the Southern Ocean to deglacial atmospheric CO2 rise****[J].* ***Nature Geoscience****, 2019, 12: 1006-1011.*

摘要：大气中二氧化碳在冰期-间冰期的变化通常归因于海水碳化学响应海洋生物地球化学和环流的大规模变化。目前，南大洋吸收的二氧化碳比其他任何地方都多，它可能在调节过去大气中的二氧化碳方面发挥了至关重要的作用。然而，在冰期-间冰期旋回期间，控制海气二氧化碳交换的物理、生物和化学变量尚未被完全了解。在这里，我们使用浮游有孔虫的硼同位素和碳同位素，以及基于烯烃的温度指标来重建过去 25000 年以来，亚南极塔斯马尼亚南部海水的 pH 值和二氧化碳分压，并研究调节海水二氧化碳的机制。新的记录显示，该地区的地表水在末次盛冰期时是大气二氧化碳的汇。我们的重建表明，生物泵强度的变化和深海二氧化碳向地表水的释放导致了末次间冰期大气二氧化碳的增加。这些发现表明，在最后一次冰期-间冰期循环期间，该区域上升流强度的变化和南大洋水团的分布对调节大气中的二氧化碳起到了关键作用。

ABSTRACT: Glacial–interglacial changes in atmospheric CO_2 are generally attributed to changes in seawater carbon chemistry in response to large-scale shifts in the ocean's biogeochemistry and general circulation. The Southern Ocean currently takes up more CO_2 than any other and it is likely to have played a crucial role in regulating past atmospheric CO_2. However, the physical, biological and chemical variables that control ocean–atmosphere CO_2 exchange during glacial–interglacial cycles are not completely understood. Here we use boron isotopes and carbon isotopes in planktonic foraminifera and an alkenone-based proxy of temperature to reconstruct seawater pH and CO_2 partial pressure in sub-Antarctic surface waters south of Tasmania over the past 25,000 years, and investigate the mechanisms that regulate seawater CO_2. The new record shows that surface waters in this region were a sink for atmospheric CO_2 during the Last Glacial Maximum. Our reconstruction suggests changes in the strength of the biological pump and the release of deep-ocean CO_2 to surface waters contributed to the last deglacial rise in atmospheric CO_2. These findings demonstrate that variations in upwelling intensity and the distribution of Southern Ocean water

masses in this sector played a key role in regulating atmospheric CO_2 during the last glacial–interglacial cycle.

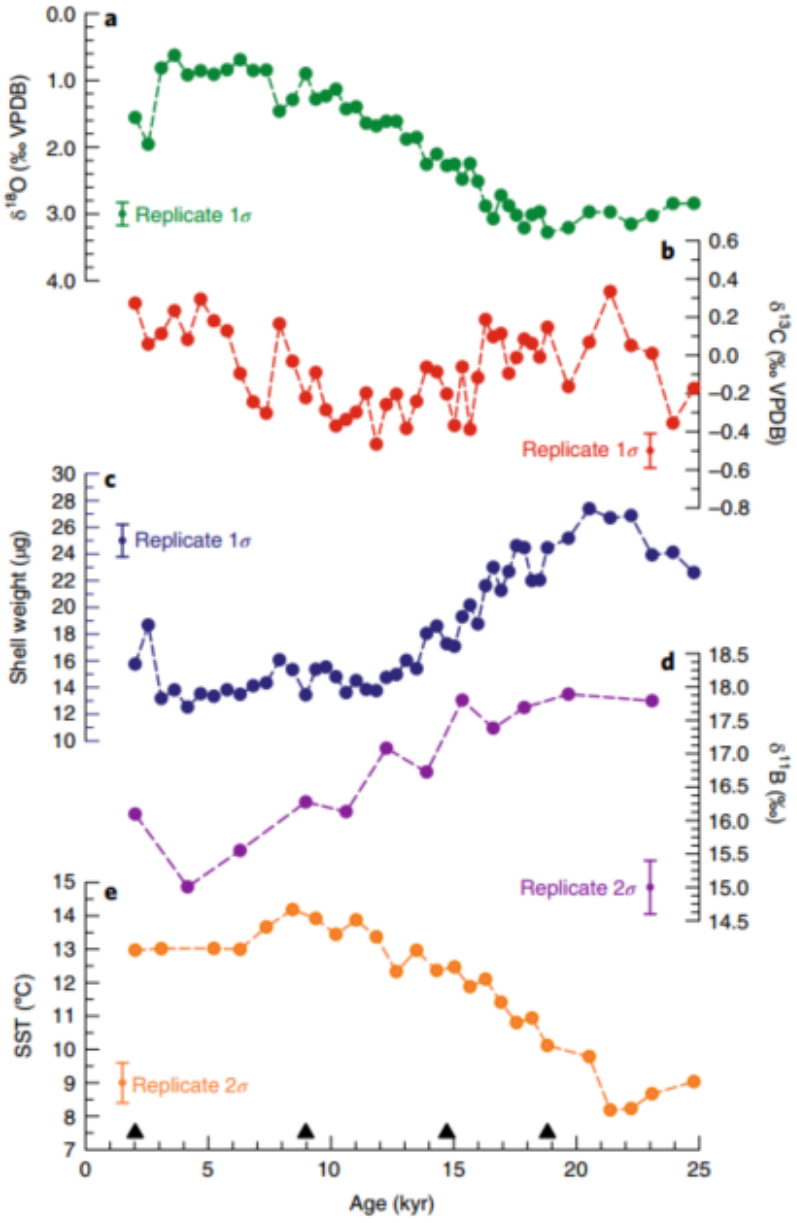

Figure 1. $\delta^{18}O$, $\delta^{13}C$, shell weight and $\delta^{11}B$ for the planktonic foraminifer,G. bulloides and SST estimates from alkenones in sediment core MD972106. a–d, Measured G. bulloides $\delta^{18}O$ (with y axis reversed) (a), $\delta^{13}C$ (b), shell weight (c) and $\delta^{11}B$ (d). e, SST estimates from alkenone unsaturation ratios ($U^{K'}_{37}$). The age model was constructed using calibrated ^{14}C ages (black triangles, Methods). Error bars represent 1σ uncertainties for $\delta^{18}O$, $\delta^{13}C$ and shell weight, and 2σ uncertainties for $\delta^{11}B$ based on replicate measurements (Methods). Error bar on the SSTs represent 2σ analytical uncertainties for replicate measurements on a homogeneous laboratory standard (Methods).

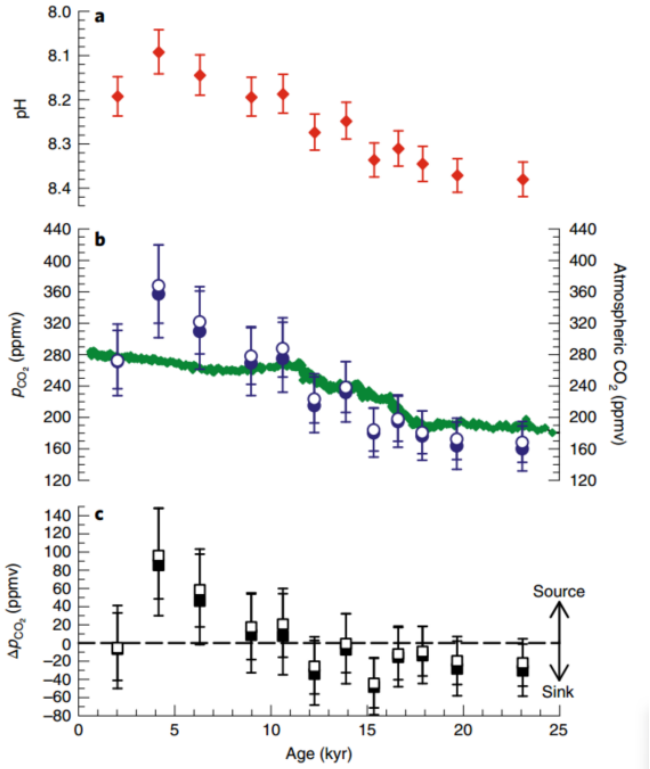

Figure 2. Reconstructed surface water pH and p CO_2 at the MD972106 site and atmospheric CO_2 over the past 25,000 years. a, Surface water pH (with y axis reversed). b, p CO_2 calculated from pH, alkenone SST and alkalinity (Method 1, solid blue circles) and from pH, alkenone SST and DIC (Method 2, open blue circles), and atmospheric CO_2 record (Antarctic ice core CO_2 composite1, green diamonds). c, Δp CO_2 is the difference between the reconstructed surface water pCO2 and atmospheric p CO_2 (ref. 1) (Method 1, solid black squares; Method 2, open black squares). Error Ibars in a, b and c represent the 95% confidence intervals around the Monte Carlo mean, where 2σ uncertainties on the individual input variables and other carbonate system parameters are propagated via the Monte Carlo simulation (n = 10,000) in the program R (Methods).

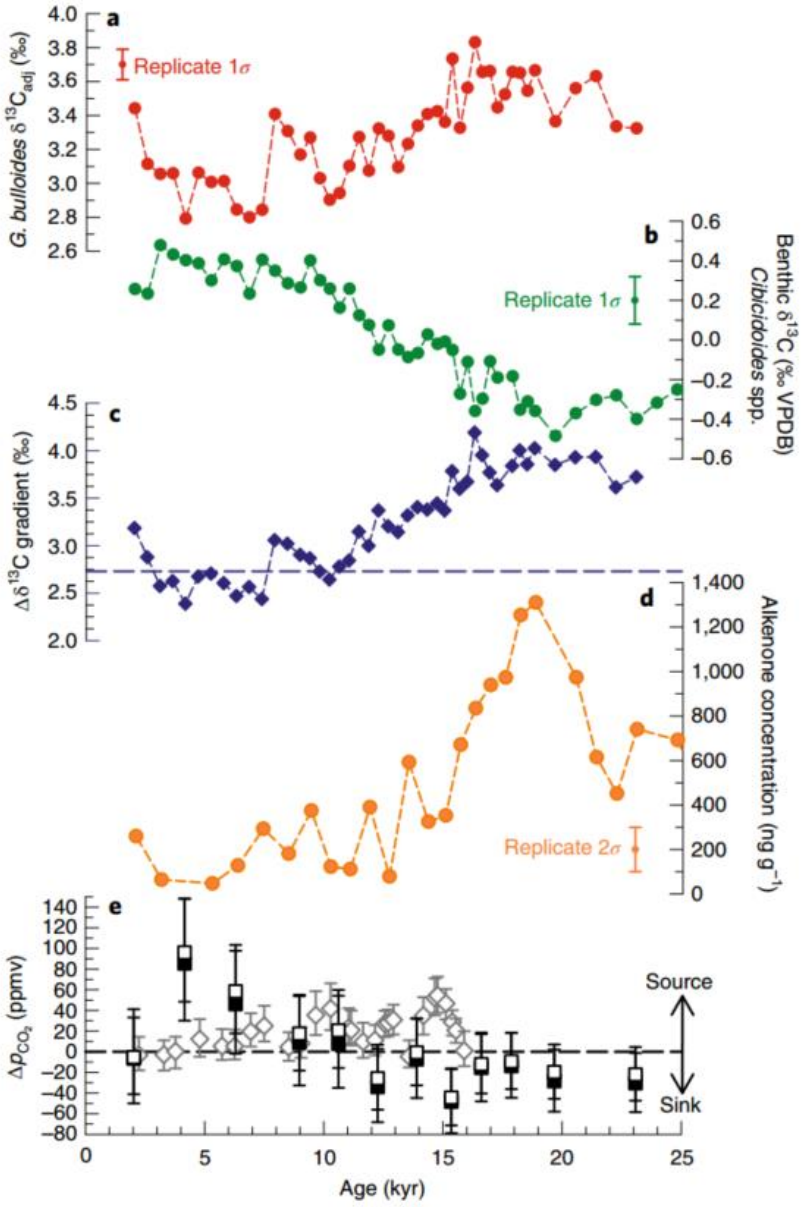

Figure 3. Planktonic and benthic foraminiferal $\boldsymbol{\delta}^{13}$C, $\boldsymbol{\Delta\delta}^{13}$C gradient, alkenone concentrations and $\boldsymbol{\Delta}p\mathrm{CO_2}$ over the past 25,000 years. **a**, $\delta^{13}C_{adj}$ for *G. bulloides*. **b**, Benthic δ^{13}C for *Cibicidoides* spp. **c**, $\Delta\delta^{13}$C gradient ($\delta^{13}C$ planktonic$_{adj}$ – δ^{13}C benthic foraminifera); the horizontal dashed line shows the average Holocene $\Delta\delta^{13}$C gradient. **d**, Alkenone concentrations. **e**, $\Delta p\mathrm{CO_2}$ is the difference between surface water $p\mathrm{CO_2}$ and atmospheric $p\mathrm{CO_2}$ (ref. 1) as in Fig. 3c. Also shown in **e** is the calculated $\Delta p\mathrm{CO_2}$ for the Atlantic sector SAZ (ref. 13) (sediment core PS2498-1 at 44° 09' S, 14° 13' 48" W, 3,783 m water depth; the grey open diamonds and error bars are the 95% uncertainty bounds). In **a**, δ^{13}C values for *G. bulloides* are temperature and $[CO_3^{2-}]$ adjusted (Methods). The error bars in **a** and **b** represent 1σ uncertainties based on replicate measurements, the error bar in **d** represent 2σ uncertainties for replicate extractions and measurements on a homogeneous laboratory standard and the error bars in **e** represent 95% confidence intervals around the Monte Carlo mean, based on 2σ uncertainties on the individual input variables and on other carbonate system parameters propagated via the Monte Carlo simulation (n = 10,000) in the program R (Methods).

6. 冰川搬运对全球铁氧化物（羟基铁）循环以及大洋输入的影响

翻译人：王敦繁 dunfan-w@foxmail.com

Raiswell R, Tranter M, Benning L G, et al. ***Contributions from glacially derived sediment to the global iron (oxyhydr)oxide cycle: Implications for iron delivery to the oceans[J]. Geochimica et Cosmochimica Acta****, 2006, 70(11):0-2780.*

摘要：对融水径流和冰山搬运输送到海洋的沉积物通量进行估算，每年大约有 2900Tg 的沉积物通过融水径流（1400 Tg/yr）和冰筏搬运（1500 Tg/yr）进入大洋中。高分辨率显微镜观察表明, 来自北极,高山,和南极位置的冰川融水中悬浮沉积物和冰山搬运的沉积物中,都含有结晶较差的铁氧化物(羟基)的纳米颗粒,大小通常约为 5nm 左右,以单一的颗粒或集合体附着在其他沉积物表面。这些纳米颗粒往往是潜在的生物可利用铁源。铁的源和汇的全球模型结果表明，冰山所携带的沉积物是向大陆架以外的开放海洋提供铁的重要来源。在最后一次冰河时期，冰山输送的含铁氧化物沉积物可能为海洋生产力的增长提供了足够的养分，而海洋生产力的增长导致了大气中的二氧化碳含量降低，这些结果可在现代冰芯记录中观察到。

ABSTRACT：Estimates of glacial sediment delivery to the oceans have been derived from fluxes of meltwater runoff and iceberg calving, and their sediment loads. The combined total (2900 Tg/yr) of the suspended sediment load in meltwaters (1400 Tg/yr) and the sediment delivered by icebergs (1500 Tg/yr) are within the range of earlier estimates. High-resolution microscopic observations show that suspended sediments from glacial meltwaters, supraglacial, and proglacial sediments, and sediments in basal ice, from Arctic, Alpine, and Antarctic locations all contain iron (oxyhydr)oxide nanoparticles, which are poorly crystalline, typically~5 nm in diameter, and which occur as single grains or aggregates that may be isolated or attached to sediment grains. Nanoparticles with these characteristics are potentially bioavailable. A global model comparing the sources and sinks of iron present as (oxyhydr)oxides indicates that sediment delivered by icebergs is a significant source of iron to the open oceans, beyond the continental shelf. Iceberg delivery of sediment containing iron as (oxyhydr)oxides during the Last Glacial Maximum may have been sufficient to fertilise the increase in oceanic productivity required to drawdown atmospheric CO^2 to the levels observed in ice cores.

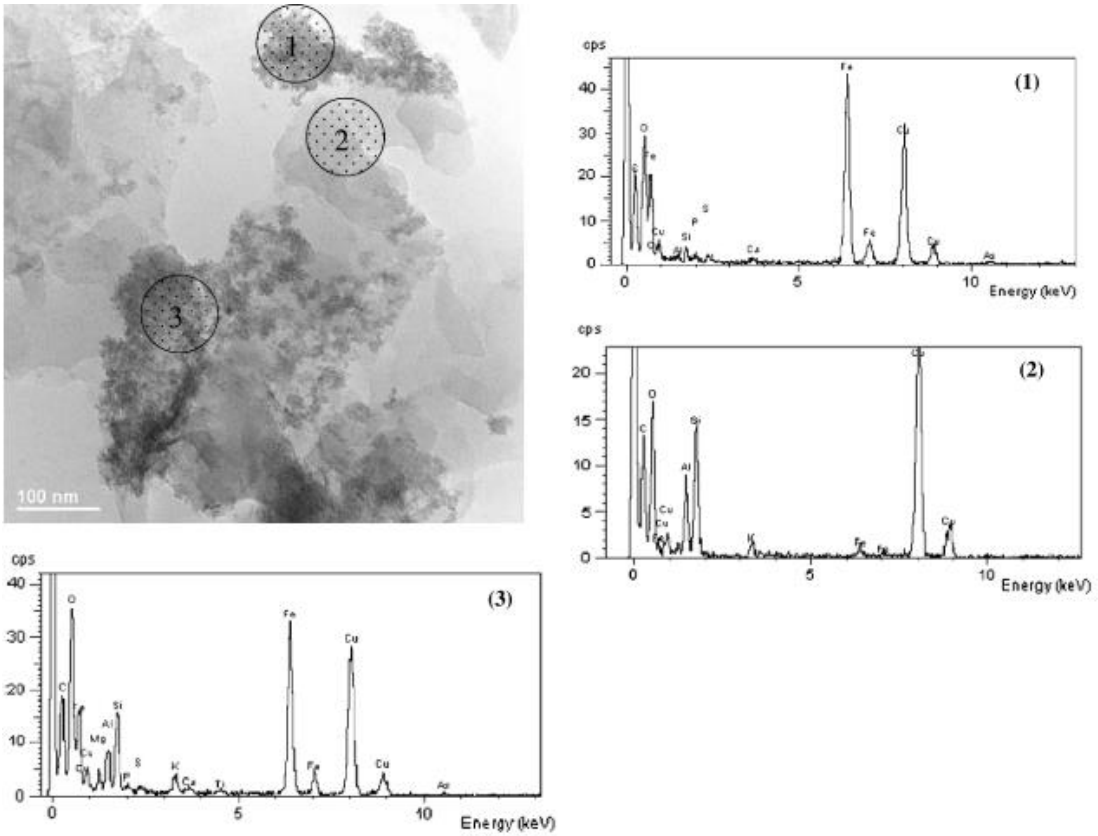

Figure 1. FEG-TEM image and EDS patterns of selected areas in the Finsterwalderbreen <2 um fraction; EDS point analyses on (1) an iron (oxyhydr)oxide cluster, (2) clay platelets, and (3) an iron (oxyhydr)oxide cluster on clays.

7. 基于不同高度磁测资料分析岩石圈磁场来源

翻译人：曹伟 11930854@mail.sustech.edu.cn

Tsvetkov Y P, Novikov K V, Ivanov A A, et al. ***Sources of the lithosphere magnetic field based on magnetic data obtained at different heights****[J].* ***Earth, Planets and Space****, 2018, 70(1): 183.*

摘要：我们的研究是基于这样一个性质，即在磁测数据中，场源深度与测量高度相等的场是最明显的。因此，磁测数据很好地反映了磁活跃层的上边界所产生的磁场(测量高度在一公里范围内)，而在高度为 20-40 公里的梯度磁测资料中，可以很好地反映出中心的地磁场。这些数据分别用于用谱方法解释岩石圈磁活跃层上边界和下边界的深度。这一事实对于估计深源的位置特别有价值。在东欧台地中部，我们通过谱方法得到的值为：该层上边界深度为 8.5km，该层下边界深度为 64.3km。通过将初始信息转换为变换后的场，向上延拓，并通过确定奇异点还原到极点的方法，实现了场源深度沿剖面的离散定位。泊松积分表示平面的外狄利克雷问题的解，为这种解释提供了理论基础。这些方法使沿着剖面更精确地确定深部磁源的位置成为可能，并表明所发表的以航空磁数据为基础的磁图并不完全包括深部磁源的磁场。

ABSTRACT：Our investigations are based on the property that the fields of sources, whose depths are numerically equal to survey heights, are most brightly presented in the data of magnetic survey. Therefore, the magnetic field created by the upper boundary of the magnetically active layer is well presented in the data of magnetic surveys (survey heights are up to the first kilometres), whereas the geomagnetic field of the centre mass is well presented in the data of gradient magnetic surveys at heights of 20–40 km. These data were used separately for the interpretation of the depths of the upper and lower boundaries of the lithospheric magnetically active layer by spectral methods. This fact is especially valuable for estimating the positions of deep sources. For the central part of the East European platform, we obtained by spectral methods, the following values: the depth of the upper boundary of the layer is 8.5 km and that of the lower boundary of the layer is 64.3 km. The discrete localisation of the source depths along the profile is performed by the methods of converting the initial information into transformed fields, continuation upward, and reduction to the pole with the determination of singular points. The Poisson integral, representing the solution of the outer

Dirichlet problem for the plane, served as a theoretical base for such an interpretation. These approaches made it possible to determine more exactly the localisation of deep sources along the profile and showed that the published magnetic maps based on aeromagnetic data do not contain in full measure the fields of deep-seated magnetic sources.

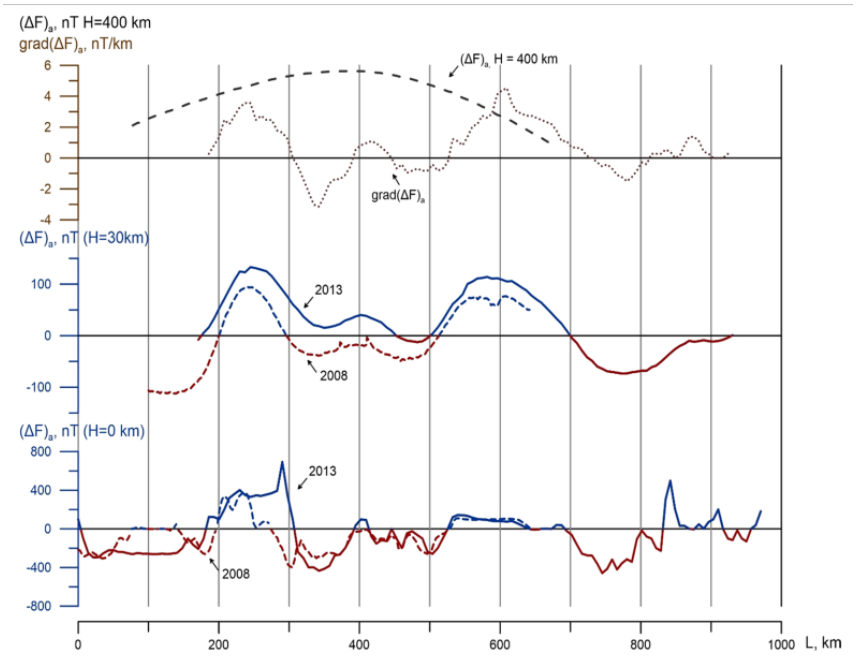

Figure 1. Data of geophysical fields along the lines of flights of stratospheric balloons in 2008 and 2013. Results of the balloon magnetic surveys performed in 2013 and 2008, as well as the intensity of the satellite KEMA (top). The data of the ground-based magnetic surveys along the routes of the balloon flights in 2013 and 2008 (bottom) taken from maps (VSEGEI 2004) showing balloon flight routes

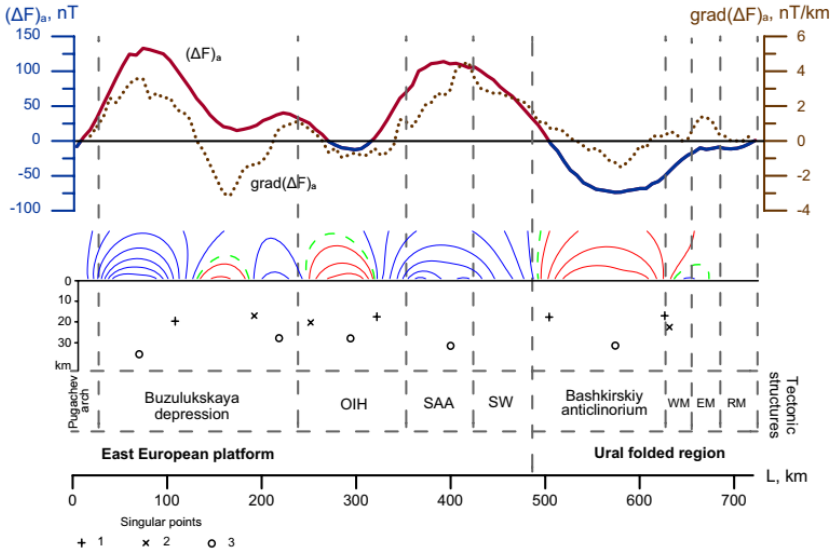

Figure 2. Example of interpretation of the results of balloon gradient magnetic surveys along the balloon flight route in 2013. OIH Orlyanka-Ivanovo structural uplift, SAA Sernovodsk-Abduleno aulacogen, SF Sterlitamak foredeep, WM West-Magnitogorsk monoclinorium, EM East-Magnitogorsk synclinorium, RF Reftinsky monoclinorium, MC Mugodzharsk-Chelyabinsk ledge

8. 美国蟑螂体内的生物磁学特征

翻译人：郑威 11930589@mail.sustech.edu.cn

Kong L J, Crepaz H, Górecka A, et al. ***In-vivo biomagnetic characterisation of the American cockroach****[J].* ***Scientific reports****, 2018, 8(1): 5140.*

摘要：本文展示了一种高灵敏度量子传感器的定量方法，该方法将磁力仪的应用扩展到处在生理温度下的生物样品，利用观察到的磁场可以无损地确定磁性物质的物理特征以及它们在样品内部的周围环境。作者将这种方法应用于美国蟑螂，揭示了在死的和活的蟑螂里的磁性沉积物有显著不同的行为。这项工作展示了活体昆虫磁动力学的第一个特征，并有助于将昆虫在磁场下的行为实验结果与它尸体中的磁性物质特征联系起来。

ABSTRACT： We present a quantitative method, utilising a highly sensitive quantum sensor, that extends applicability of magnetorelaxometry to biological samples at physiological temperature. The observed magnetic fields allow for non-invasive determination of physical properties of magnetic materials and their surrounding environment inside the specimen. The method is applied to American cockroaches and reveals magnetic deposits with strikingly different behaviour in alive and dead insects. We discuss consequences of this finding to cockroach magneto-reception. To our knowledge, this work represents the first characterisation of the magnetisation dynamics in live insects and helps to connect results from behavioural experiments on insects in magnetic fields with characterisation of magnetic materials in their corpses.

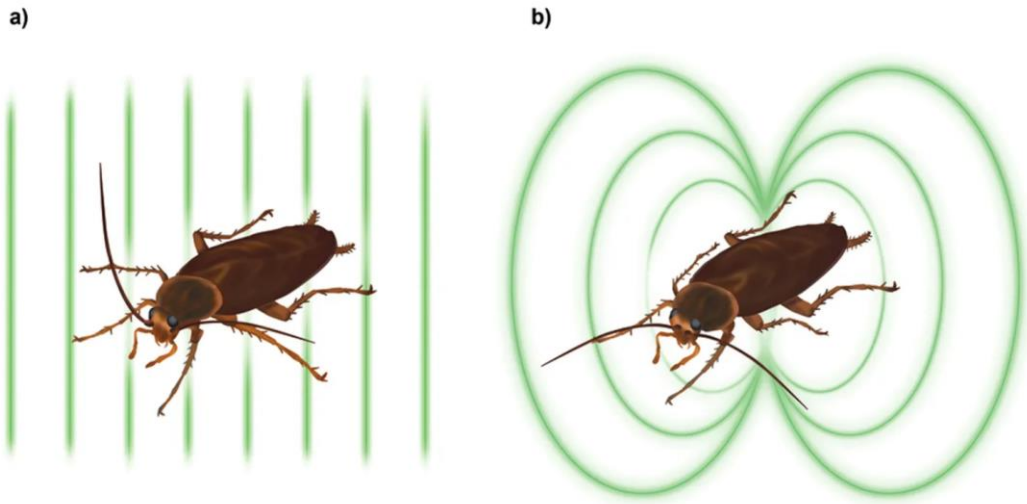

Figure 1. Sketch of the experiment. (a) American cockroaches were placed in a strong magnetic field aligned perpendicular to the thorax as illustrated by the green lines. Using an atomic magnetometer we monitored the dynamics of the magnetic field generated by the magnetised insects. (b) The magnetic field is very close to the field of magnetic dipole normal to the thorax. Published with permission from T. Yeo.